Engineering with Computers
https://doi.org/10.1007/s00366-024-01979-z

ORIGINAL ARTICLE

Isogeometric analysis of architected materials and structures

Ke Ma[1] · **Yuri Bazilevs**[1]

Received: 16 January 2024 / Accepted: 3 April 2024

Abstract
In recent years, architected materials and structures have gained significant popularity due to their ability to reach enhanced performance for use in multifunctional and multidisciplinary applications. Among numerous options investigated, architected structures based on Triply Periodic Minimal Surfaces (TPMS) have gained increasing attention because they exhibit exceptional properties in multiple disciplines simultaneously. However, because of the complexities involved in the geometry representation and mechanical response of these structures, physics-based modeling for this problem class engenders a set of challenges. In this paper we address some of these challenges by developing a first-of-its-kind Isogeometric Analysis (IGA)-based geometry modeling and simulation framework for architected materials and structures. We focus on sheet TPMS-based structures, for which we first develop an IGA-suitable geometry modeling pipeline and then evaluate their mechanical performance in crushing simulations employing Isogeometric shells based on the Kirchhoff–Love (KL) theory.

Keywords Architected materials and structures · Isogeometric analysis (IGA) · Triply periodic minimal surfaces (TPMS) · Non-uniform rational B-splines (NURBS) · Kirchhoff–Love shells · Protective structures

1 Introduction

Two-dimensional slices through material-property space yield material-property charts or so-called "Ashby charts" [1]. Each chart has material properties as two axes and is populated with engineering materials. The remaining white spaces, if accessible, drive scientists to design and produce novel materials with a desired combination of properties. The traditional approaches create new metal alloys, polymers, and compositions of glass and ceramics by way of chemistry. Taking one step further, Ashby and Bréchet proposed developing hybrid materials by combining two or more materials such that their properties are superposed. As a successor of hybrid materials, the term "architected materials" places an emphasis on the control over the material architecture. Architected materials and structures are designed using a special and preferably optimal combinations of materials and open spaces, i.e., architectural features. Such new materials are configured to reach enhanced performance for use in multifunctional and multidisciplinary applications resulting in breakthrough developments in solving key societal challenges [2].

To showcase the state-of-the-art in architected materials and structures, silicon-coated tetragonal microlattices are designed with programmable patterns in response to electrochemical lithiation through cooperative beam buckling caused by artificial defects [3]. This is a vivid exemplar of leveraging microstructural instabilities [4] to control macroscopic performance and achieve novel functionality. Aside from a multitude of studies on mechanical properties such as stiffness and strength, insights into damage tolerance capabilities and recoverability are provided. The notion of fracture toughness is extended first to octet-truss lattices [5] and then to truss-based metamaterials [6]. This opens the way to fracture behavior characterization for architected materials and structures. Excellent resilience is revealed in the hierarchical architected metamaterials with recoverability up to 98% after compression, where non-axially oriented beams play a major role [7]. At the nanoscale, the diffusion of point defects in single-crystalline nanowires [8] and thin-shell nanolattices [9] results in a similar property defined as anelasticity, where the structures gradually recover from deformation after unloading. Recently, architected metamaterials

✉ Yuri Bazilevs
yuri_bazilevs@brown.edu

Ke Ma
ke_ma@brown.edu

[1] School of Engineering, Brown University, 184 Hope Street, Providence, RI 02912, USA

Published online: 23 April 2024

inspired by the art of origami also displayed remarkable shape recoverability, mainly at the microscale [10].

Among numerous architected materials, those based on triply periodic minimal surfaces (TPMS) [11] exhibit a favorable integration of properties and the resulting performance merits. To name a few, TPMS-based structures can serve as heat exchangers and temperature controllers owing to the highly smooth surfaces and large surface area to volume ratio [12]. For similar reasons, they are also good candidates for catalysts and reactors in chemical industries [13]. In addition to the aforementioned properties, TPMS-based structures are highly interconnected. As such, they have successfully been used as tissue engineering scaffolds and medical implants since they provide enough space for efficient transport of nutrients and waste for cell growth [14]. More relevant to the present work, the response of TPMS-based structures to extreme loading conditions justify their use as energy and impact absorbers [15]. In particular, unlike in truss-based lattice structures, the smooth geometry of TPMS avoids stress concentrations and exhibits a more ductile response allowing the structure to mitigate extreme loading through significant continuous plastic deformation.

The objective of the present research is to develop a modeling framework for architected materials and structures focusing on sheet TPMS-based designs and applications involving protective structures that can mitigate the effect of extreme loading. Sheet TPMS structures are obtained by offsetting the TPMS in the surface-normal direction with a given thickness value. As such, they can be idealized and modeled as shell structures [16]. To handle the geometric complexity and advanced nature of the mechanics involved, we propose to develop the framework based on Isogeometric Analysis (IGA) [17, 18]. The key strength of IGA is the inherently tight integration between design and physics-based modeling, which enables efficient simulation-based design of TPMS structures for a desired set of performance characteristics, before these are handed off to manufacturing (typically through additive manufacturing techniques) for further experimental testing or for production. Because we focus on sheet TPMS structures, we additionally leverage recent developments in IGA-based shells [19, 20]. In the past decade the IGA shell technology was shown to surpass traditional Finite Element (FE)-based [21, 22] approaches in terms of per-degree-of-freedom accuracy and robustness in modeling large-deformation inelastic behavior with self-contact. These characteristics of IGA-based shells make them ideal candidates for the present application.

The remainder of the manuscript is structured as follows. In Sect. 2, we develop an IGA-suitable modeling framework for sheet TPMS structures, where the shell surfaces are represented using Non-Uniform Rational B-Splines (NURBS) [23]. A short description of the IGA-based Kirchhoff–Love (KL) shell formulation is presented in Sect. 3. Numerical simulations of sheet Primitive TPMS-based structures subjected to compressive loading are shown in Sect. 4, including mesh refinement studies for unit cells and experimental validation for lattices. In Sect. 5, we draw conclusions and outline future research directions.

2 IGA-based framework for sheet TPMS structures

In this section, we present in detail a pipeline for generating IGA-suitable geometric models of sheet TPMS structures. The resulting models may be used directly in IGA-based shell analysis described in the later sections of this paper.

2.1 TPMS

Originating from soap-film phenomena, minimal surfaces minimize their total surface area under some constraints, which is mathematically equivalent to having zero mean curvature. A TPMS is defined as a minimal surface that is periodic in three independent directions. The three-fold periodicity is used to generate lattices through the repetition of unit cells. Furthermore, a TPMS is an isosurface and thus can be represented by an implicit equation of the form $f(x, y, z) = C$. Table 1 presents the mathematical descriptions of three common types of TPMS, Primitive (P), Gyroid (G) and Diamond (D), where x, y, z are the spatial coordinates, w_x, w_y, w_z are the ratios of 2π and the side lengths of the bounding cell in their respective directions, and C on the right side of each equation is a level constant that controls the pore size. The resulting unit-cell and $4 \times 4 \times 4$-lattice shapes are also shown to illustrate the effect of choosing different $f(x, y, z)$. In the present work we will focus on a TPMS of Primitive type, which was first described in Schwarz [24] and then named by Schoen in his seminal technical note [11]. Earlier work on this type of TPMS laid the foundations for the modeling procedures of sheet Primitive TPMS-based structures, as will be discussed in what follows.

2.2 Minimal patch

We introduce a concept of a "minimal patch" which is part of the Primitive TPMS unit cell that will be represented using a single NURBS patch in the IGA model. The full unit cell is then constructed by rotation and mirroring operations and connecting the minimal patches, represented with NURBS, using C^0 continuity. In order to identify the minimal patch, we first determine the so-called "fundamental patch". A fundamental patch is the smallest part of the unit-cell surface from which the full unit-cell surface can be constructed through rotation and mirroring operations.

Table 1 Three common types of TPMS

Type	Name	Mathematical expression	Unit cell	$4 \times 4 \times 4$ lattice
P	Primitive	$f_{\mathrm{P}}(x,y,z) = \cos(w_x x) + \cos(w_y y) + \cos(w_z z) = C$	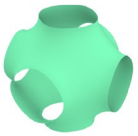	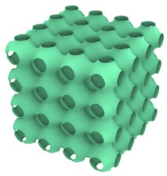
G	Gyroid	$f_{\mathrm{G}}(x,y,z) = \sin(w_x x)\cos(w_y y) + \sin(w_y y)\cos(w_z z) + \sin(w_z z)\cos(w_x x) = C$	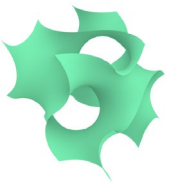	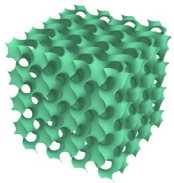
D	Diamond	$f_{\mathrm{D}}(x,y,z) = \cos(w_x x)\cos(w_y y)\cos(w_z z) - \sin(w_x x)\sin(w_y y)\sin(w_z z) = C$	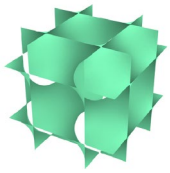	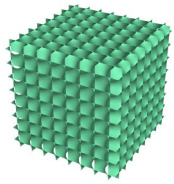

Figure 1a–e illustrate a procedure of finding the minimal patch. Taking advantage of cubic symmetry [25], the unit cell with its bounding cell (see Fig. 1a) is decomposed into eight sub-cells as shown in Fig. 1b. Figure 1c zooms on a bounding sub-cell facing the reader and shows a piece of the surface that is fully contained in it. At this stage, a "kaleidoscopic cell" is introduced, which is defined as a convex polyhedron enclosing the fundamental patch via planar boundaries [26]. In the case of Primitive TPMS, the kaleidoscopic cell arizes from further subdivision of the bounding sub-cell in Fig. 1c into six quadrirectangular tetrahedra as illustrated in Fig. 1d. One such tetrahedron enclosing the fundamental patch is shown in Fig. 1e. In principle, the fundamental patch may be taken as the minimal patch in order to construct the NURBS surface of the unit cell. However, in order to minimize the number of NURBS patches and C^0-continuous interfaces between them, two fundamental patches are combined to define the minimal patch as shown in Fig. 1f. This construction results in 24, as opposed to 48, minimal patches per unit cell and a dramatic reduction in the number of C^0-continuous interfaces, which improves efficiency of the computations and quality of the results.

2.3 Implementation of the modeling framework

Here we outline a framework and its implementation for the generation of IGA-suitable models of sheet TPMS structures. Following the approach in [27], we propose a solution that tightly integrates a Computer Aided Design (CAD) software Rhinoceros® (often abbreviated as "Rhino") [28]

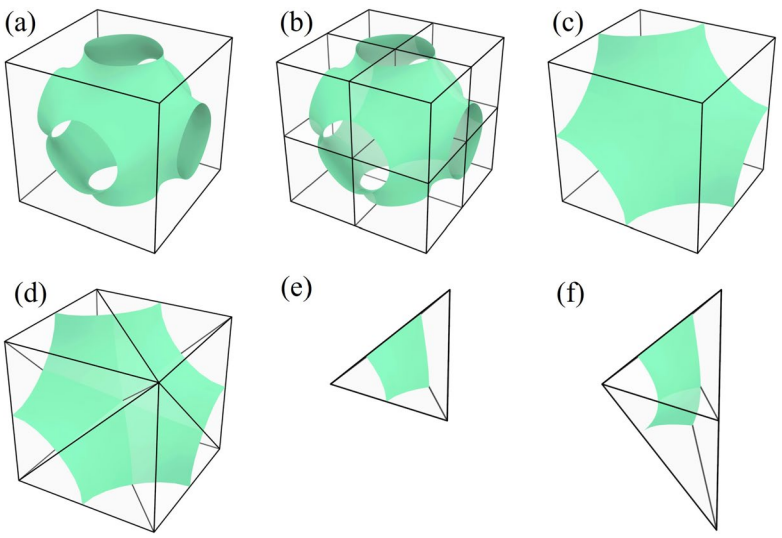

Fig. 1 **a**–**e** Sequence of bounding-cell subdivisions leading to the fundamental patch; **f** Minimal patch obtained by combining two fundamental patches

and a graphical programming design tool Grasshopper® [29]. Rhino provides the modeler with a rich array of functions that are used to generate complex, multi-patch NURBS surfaces, while Grasshopper enables visual programming in terms of components with predefined functionality and wire connections between the components as conduits of input and output data. The five main steps of the geometry modeling framework are outlined in Fig. 2, while the Grasshopper components used in each step and grouped inside purple rectangles are shown in Fig. 3. Labels for each of the five steps and the Grasshopper components are provided in boldface font in the figures. The solid and dashed wires between the components indicate input and output relations.

In the first step, a mathematical expression of the Primitive TPMS is explicitly included in the yellow "Panel" component, while the component "Center Box" defines the bounding cell (see Fig. 3). It is important that the bounding cell is consistent with the arguments of the implicit equation for the TPMS surface. The "level constant" controlling the pore size and "target count" regulating the density of interpolation points are the two remaining inputs of the Python script that extracts a grid of interpolation points of the minimal patch. In the present case, the half-side lengths are set to 4 mm in each direction, the default *xy* plane is set as the base, and the level constant is set to zero. The resulting minimal patch expressed as a grid of spatial points is shown in Fig. 4a. The bounding cell is also part of the output as it will be used in the later steps.

Next, the Python script takes as inputs the interpolation points, the bounding cell, and the polynomial degrees in the parametric (i.e., u and v) directions and creates a NURBS surface of the minimal patch. Figure 4b shows the NURBS surface resulting from the grid of interpolation points in Fig. 4a. The algorithm titled "NurbsSurface.CreateThroughPoints", which is internal to Rhino, is employed to generate the NURBS surface from point data. The accuracy of the surface fitting algorithm is discussed in Sect. 4.

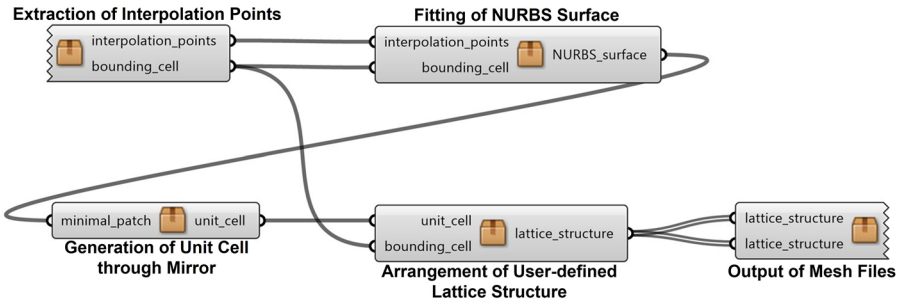

Fig. 2 Five main steps of the IGA-suitable geometry modeling framework

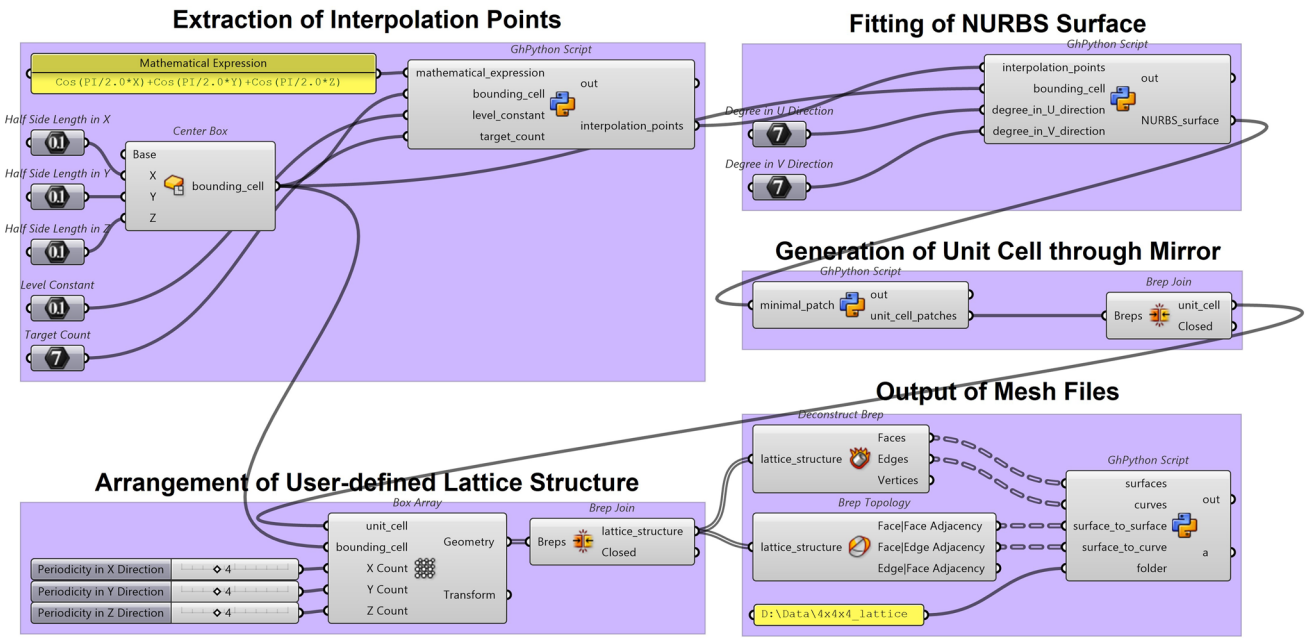

Fig. 3 Grasshopper components and connections implementing the IGA-suitable geometry modeling framework

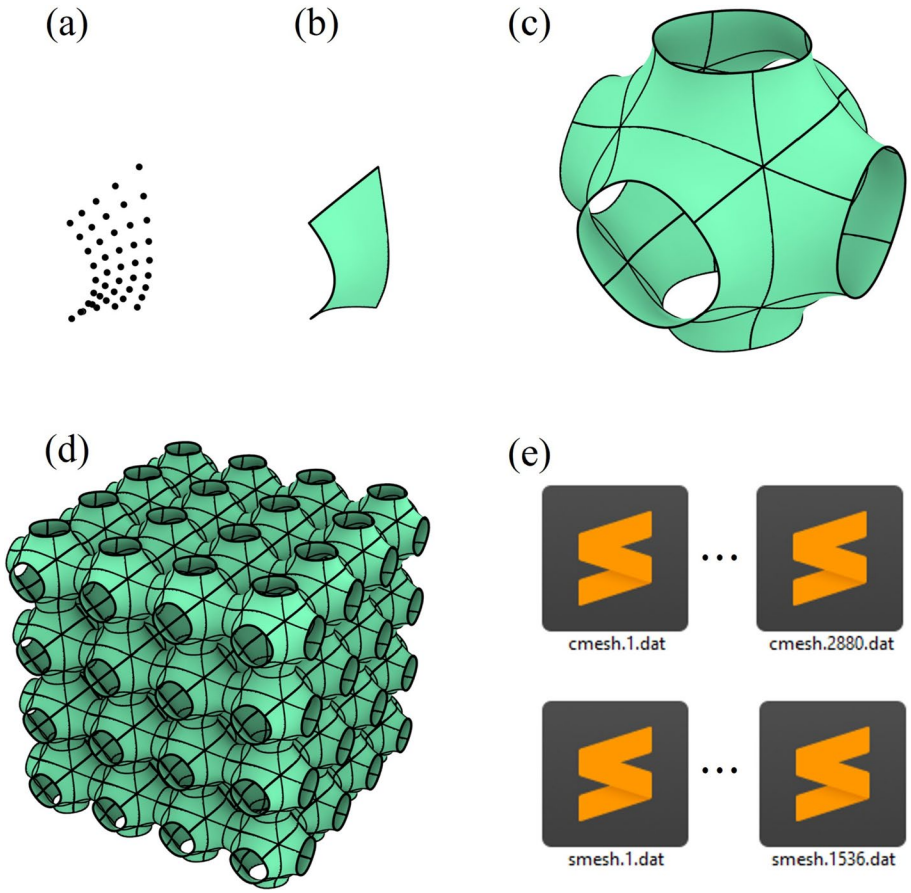

Fig. 4 Output of each step of the IGA-suitable geometry modeling framework

A series of mirror operations gathered in the Python script of the third step are applied to the NURBS surface of the minimal patch, generating 24 untrimmed and conforming patches of the TPMS unit cell. The component "Brep Join" merges the patches into a multi-patch NURBS surface, which is shown in Fig. 4c. As the next step, a number of unit cells is specified in each periodic direction, which is implemented through the component "Box Array". The output is followed by a second "Brep Join" component to merge the unit cells into a single surface. Figure 4d shows the resulting NURBS model of the sheet TPMS structure assuming four unit cells in each direction.

In the final step, the mesh files are formatted consistent with the data structure of the IGA-based KL shell code used for the computations. A brief review of the KL shell formulation employed is provided in Sect. 3. The component "Deconstruct Brep" deconstructs the NURBS model into faces, edges and vertices. The faces (i.e., surfaces) and edges (i.e., curves) are used as inputs of the Python script. Another component "Brep Topology" has two additional outputs: surface-to-surface and surface-to-curve adjacency. It is important to note that this information is inaccessible without the use of two "Brep Join" components in the previous steps. This adjacency data is needed to construct the so-called penalty curves used to carry out the integrals to enforce rotational continuity between the adjacent patches in the KL shell formulation. The yellow "Panel" component points to the folder where two types of mesh files are be written, one for the patches and another for the penalty coupling curves. The mesh files contain the usual data for IGA-based computations including polynomial degrees, knot vectors and control points (coordinates and weights). The penalty curve mesh files also include the indices of two adjacent patches. Figure 4e shows the file layout for our $4 \times 4 \times 4$ lattice structure with 1536 mesh files for the patches and 2880 mesh files for the penalty coupling curves.

2.4 Advantages and extensions

The proposed IGA-based model generation framework summarized in Fig. 3 presents a tight integration between design and simulation and gives the following advantages over more traditional FEM-based procedures. First, the analysis-suitable models are generated exclusively using the Rhino-Grasshopper framework, without the need to bring in additional software and to deal with time consuming and error prone data formatting. Second, the modeling process is flexible enough to fit different targets. For example, a variety

of TPMS types may be specified by simply retyping the analytical expression of the implicit function $f(x, y, z) = C$. Third, model revisions may be achieved anytime during the geometry construction process, i.e., on the fly, which reflects the stability of spline interpolation and robustness of algorithmic implementation. Above all, convenient parametric control of the sheet TPMS structure geometry is achieved at very little cost.

The framework also enables tight control over NURBS mesh design. The number of NURBS control points for a minimal patch is controlled by the target count, which is an input parameter. The polynomial order of the NURBS mesh is also a simple input parameter. As a result, a sequence of unit cell models with an increasing number of control points per minimal patch is easily constructed using the framework developed. This makes it relatively straightforward to carry out mesh refinement/convergence studies and to assess the effect of mesh resolution on the quantities of interest in the simulations for a unit cell, before focusing on the more expensive lattice-level calculations.

The framework developed allows several extensions that we plan to pursue in the future work. We anticipate the same level of parametric control over the architectures of other TPMS-based structures, including geometrically and/or functionally graded designs as well as lattices with customizable external shapes, all of which are of significance in a variety of engineering and science applications [30]. For example, Fig. 5 shows a sheet Primitive TPMS lattice cut into a cylindrical shape using Boolean operations.

3 IGA-based KL shells

The work on IGA-based shells began with two seminal contributions, covering the thin or shear-rigid case [19], generally referred to as the KL shell, and the thick or shear-deformable case [20] generally referred to as the Reissner–Mindlin (RM) shell. In several subsequent contributions [31–35] it was demonstrated that IGA gave superior robustness for large deformations and accuracy per degree of freedom (DoF) compared to more traditional FE-based approaches. In addition, a KL shell formulation in terms of mid-surface displacement DoFs requires higher continuity of the approximation spaces, which makes it especially well suited for treatment by IGA. (Alternatively, KL shells were formulated in terms of subdivision-surface discretizations in [36] and, more recently, using meshfree methods in [37].) In the present work, we focus on KL shells.

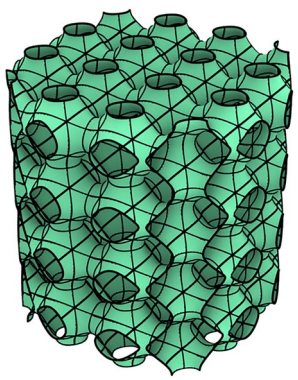

Fig. 5 Primitive TPMS lattice with a cylindrical external shape

A general-purpose IGA-based KL shell formulation from [38] is employed here for the dynamic analysis of sheet TPMS structures undergoing large elasto-plastic deformations. Motivated by the degenerated solid approach [31, 32, 39, 40], the formulation makes use of the Updated Lagrangian form of the 3D solid governing equations where the kinematics is subjected to the constraints of the KL shell theory. The assumptions of KL shell kinematics give rise to a special form of the velocity gradient operator that is central to the discrete weak formulation, which uses a conventional Galerkin discretization using NURBS and implicit midpoint time integration. Constitutive laws are implemented in terms of the Green–Naghdi rate of the Cauchy stress [22]. The stress update is carried out in the co-rotational frame where the rotation tensor is updated using the algorithm of Flanagan and Taylor [41]. The zero through-thickness stress condition is enforced iteratively as part of the stress update step. A non-local penalty-based formulation from [42] is used to handle contact, including self-contact occurring during the lattice crushing simulations.

To account for rotational continuity at patch interfaces, a penalty method is employed due to its simplicity and efficiency [43, 44]. Alternatively, one may use a bending-strip method [45], a blended-shell formulation that selectively introduces rotational DoFs at patch interfaces [32], a mortar technique [46, 47], or Nitsche's method [48, 49] for patch coupling. We note that the bending-strip technique was the first general-purpose methodology for patch coupling that enabled the application of KL shells to geometrically-complex real-life structures.

A traditional J_2 elasto-plastic constitutive law with isotropic hardening is employed in the present work to model the material behavior of stainless steel 316 L (SS316L). In [50], standard tension tests were carried out to characterize the mechanical behavior of the SS316L material, which, in turn, was used in [51] to fabricate sheet TPMS lattice specimens and carry out quasi-static compressive loading experimental tests. The results of these tests will be used for the purposes of validating our modeling and simulation framework. Based on the mechanical characterization data from [50], we set Young's modulus to 190 GPa. A nonlinear isotropic hardening law takes the form $K(\bar{e}_p) = \sigma_y^0 + (\sigma_y^\infty - \sigma_y^0)(1 - e^{-\beta\bar{e}_p}) + \alpha\bar{e}_p$, where K is the yield stress and $\bar{e}_p$ is the effective plastic strain. The hardening-law parameters employed in the computations are

summarized in Table 2. Poisson's ratio is set to 0.3, which is a typical value for steels. Experimental tests in [51] indicate that while the specimens undergo large plastic deformation, no significant material failure is present. As such it is felt that using a plasticity model without failure is sufficient for the present simulations.

4 Computational results

In this section, the capabilities of the IGA-suitable geometry modeling framework coupled with the KL shell solver are demonstrated through a series of large-deformation inelastic calculations of sheet TPMS-based lattice structures subjected to quasi-static compression. We first carry out a mesh convergence study of a single Primitive TPMS unit cell to assess the resolution requirements for the present application. We then carry out the calculations of $4 \times 4 \times 4$ lattices. We assess the effect of shell thickness on the mechanical response of the lattice structures by considering the unit cells with relative density of about 20%, 10% and 5%. Given the unit cell dimension of 4 mm, these correspond to shell thickness values of 0.282 mm, 0.128 mm and 0.085 mm taken from [51]. All the computations employ C^1-continuous quadratic NURBS basis functions at the patch level. Uniformly reduced 2×2 Gaussian quadrature rule is employed in the mid-surface for better efficiency and to alleviate possible membrane locking [52]. However, shell thickness appears to be in the range where membrane locking is not expected to have a significant effect. Three quadrature points through the thickness direction are employed, which is important to capture plasticity arizing from bending-dominated deformation in the present application.

Table 2 Parameters of the nonlinear isotropic hardening law employed in the computations

σ_y^0	σ_y^∞	β	α
450.0 MPa	565.0 MPa	10.7	655.1 MPa

4.1 Unit cell computations: mesh refinement study

The 24 patches of a unit cell are labeled as neck, shoulder and body patches relative to the load direction as shown in Fig. 6a. A mesh refinement study is carried out for a unit cell discretized using $9 \times 5, 11 \times 6, 13 \times 7$, and 15×8 control points per minimal patch. Boundary conditions are illustrated in Fig. 6b. The top and bottom two rows of control points, marked in the figure, are assigned essential boundary conditions as follows: The bottom two rows are fixed in all three spatial directions; the top two rows are fixed in x- and y-directions and a constant downward velocity of 1 m/s is applied in the z-direction.

Figure 7 shows the accuracy of the surface approximation using a minimal patch with $9 \times 5, 11 \times 6, 13 \times 7$, and 15×8 control points. Here, the horizontal axis shows the inverse of the normalized mesh size $1/\tilde{h}$ and the vertical axis shows the L^2-norm of the error in the normal vector normalized by the square root of the surface area, namely:

$$e = \frac{\left[\int_A (\boldsymbol{n} - \boldsymbol{n}^h) \cdot (\boldsymbol{n} - \boldsymbol{n}^h)\, dA\right]^{1/2}}{\left(\int_A dA\right)^{1/2}} \times 100\%. \tag{1}$$

The symbol $\boldsymbol{n}$ denotes an exact normal vector calculated from the analytical expression of the TPMS and $\boldsymbol{n}^h$ denotes the normal of the resulting NURBS surface. Despite the fact

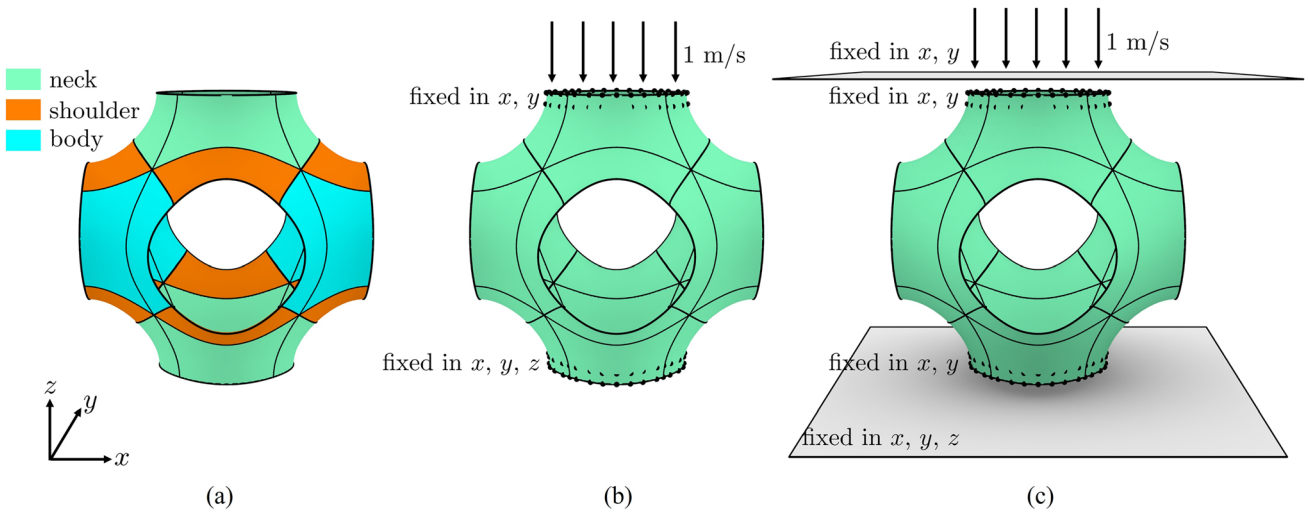

Fig. 6 Patch labels, problem setup and boundary conditions

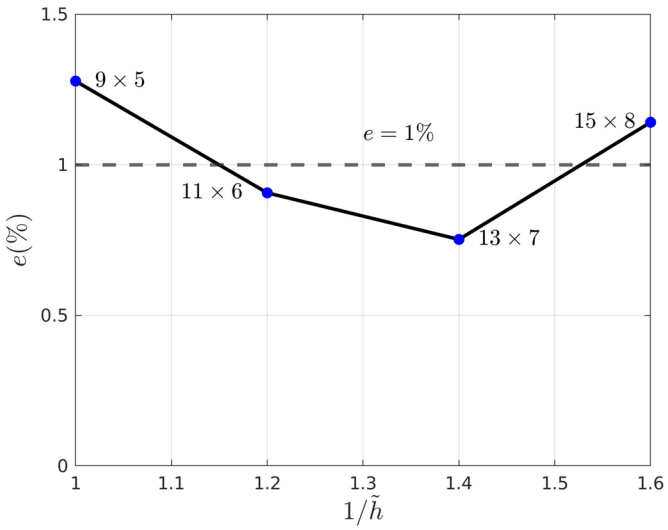

Fig. 7 Normalized L^2-norm of the error in the normal vector expressed in %

that the number of interpolation points matches the number of NURBS basis functions for the minimal patch, the relative error saturates at about 1%. Because the interpolation procedure is internal to Rhino, we are not able to pinpoint the origins of this error saturation.

Figure 8 shows the nominal stress–strain curves for the four meshes and three relative densities. The nominal stress is defined as the total reaction force in the z-direction summed over the top two rows of control points divided by the transverse area of the bounding cell; the nominal strain is

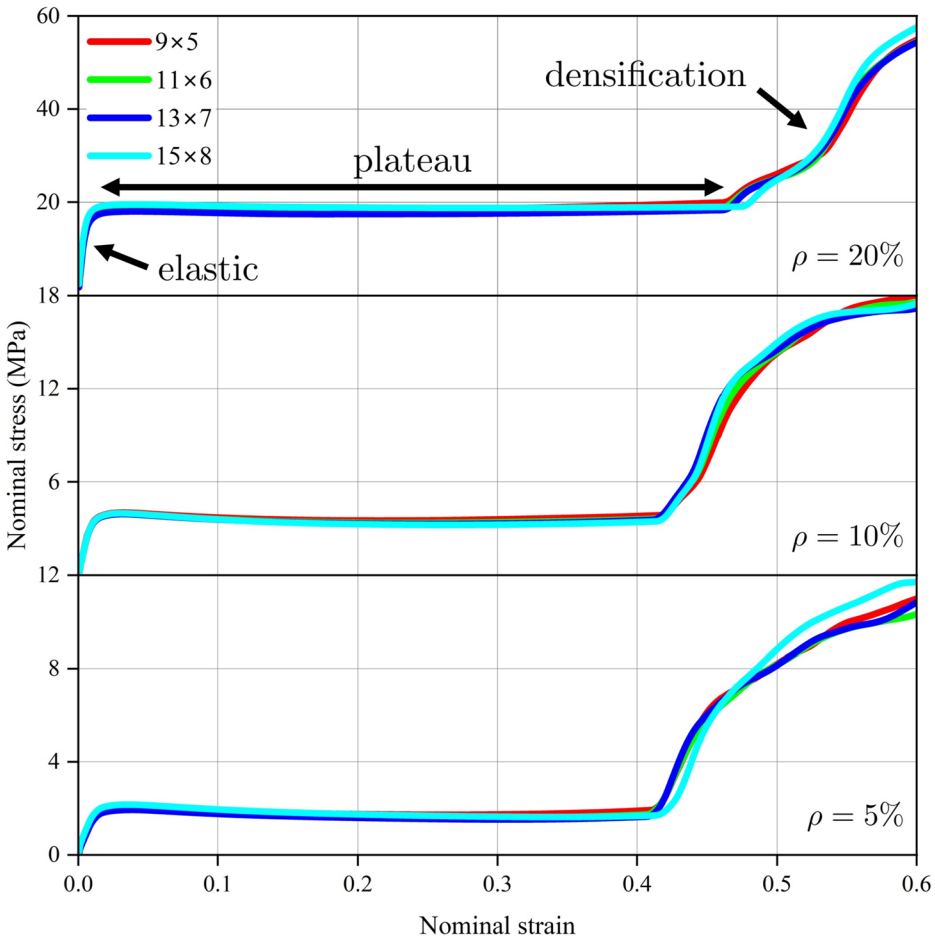

Fig. 8 Nominal stress–strain curves for the four meshes and three relative densities

calculated by dividing the compressive displacement by the original height of the bounding cell. Taking the case of 20% relative density as an example, we illustrate the three typical regions of the load–displacement curve: elastic region, plastic plateau region, and densification region. The elastic region, showing essentially linear stress–strain response, is very short. Plastic deformation appear shortly after, indicating the start of the plastic plateau region where nominal stress stays at a nearly constant value for a wide range of strain values. The long plastic plateau manifests the ability of the structure to absorb energy through plastic deformation at constant stress and serves as an important indicator in evaluating crashworthiness [53]. The densification region that follows is marked by a rise in the nominal stress, which is mainly due to self-contact that is activated at high levels of compression. For the 10% and 5% relative density cases the shape of stress–strain curves is very similar to the 20% case. It is also important to note that the stress–strain curves are all very similar between the four meshes considered. As a result, in what follows, we will use the 9×5 mesh of the minimal patch for all the lattice-level calculations.

Figure 9a shows the snapshots of equivalent plastic strain at different levels of compression for the thickest case using the 9×5 mesh for the minimal patch. The neck, shoulder and body patches play different roles in the compressive deformation process. The neck patches experience little plasticity and deformation until after self-contact activates at about 50% effective strain. Shoulder and body patches plasticise essentially from the start of compression. Body patches undergo significant bending deformation and develop high equivalent plastic strain. The deformation of shoulder and body patches governs the shape of the side boundaries during compression. The side boundaries start as approximate circles. With more deformation they take on an elliptical shape and eventually form lobe structures, which were experimentally observed in [54] and illustrated in Figure 9b.

4.2 Experimental validation

The $4 \times 4 \times 4$ lattice computations were set up and carried out using a similar combination of clamping and prescribed velocity boundary conditions. Figure 10 shows a final configuration of the 20% relative density case. While the overall deformation is reasonable, we note that due to the lack of top and bottom restraining plates the deformation of the edge cells is abnormal. For this reason, we added the end plates to the model, which restrict the vertical motion and better mimic the experimental setup. The added end plates have 0.5 mm thickness and are assumed to be rigid. Compression of the structure is now driven by introducing additional contact between the end plates and TPMS core, which is also handled as self-contact. The bottom plate is fixed in all directions, while the top plate is fixed in x- and y-directions and driven by a constant downward velocity of 1 m/s in the z-direction. The top and bottom two rows of control points of the TPMS core are also fixed in the x- and y-directions to mimic friction between the end plates and test specimen. Figure 6c illustrates the setup for a single unit cell, which is easily extrapolated to the full lattice case. Note that the nominal stress is now calculated from the total z-direction contact force on the top plate.

The nominal stress–strain response for the relative densities of 20%, 10% and 5% is plotted in Fig. 11. Comparison with the experimental data from [51] is also provided in the plots. The computations are carried out until the compression level reaches 80% nominal strain. The ability of IGA to

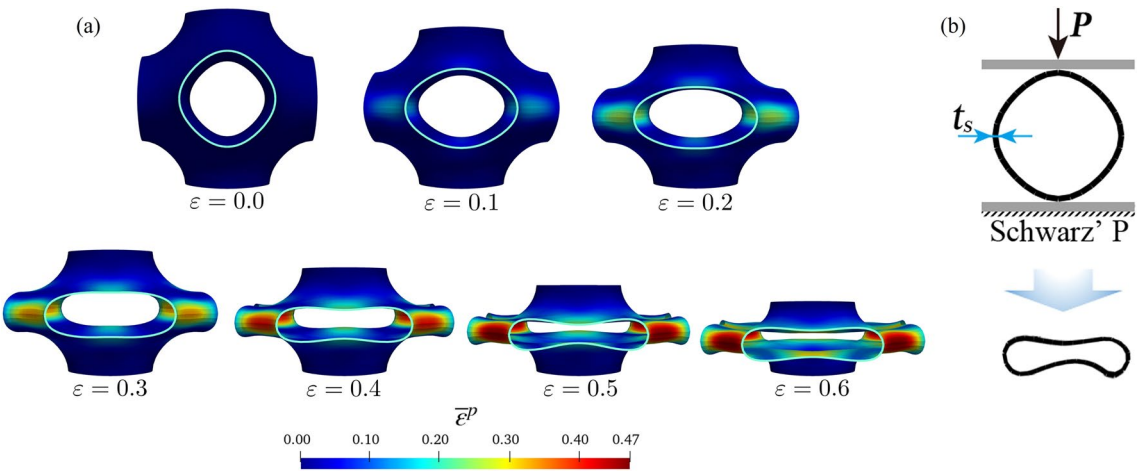

Fig. 9 **a** Equivalent plastic strain plotted on the deformed configuration at different levels of compression. Here, $\rho = 20\%$ and the minimal patch is discretized using 9×5 control points; **b** Side boundaries with near circular shape in the undeformed configuration develop lobe structures in compression. Experimental observations are from [54]

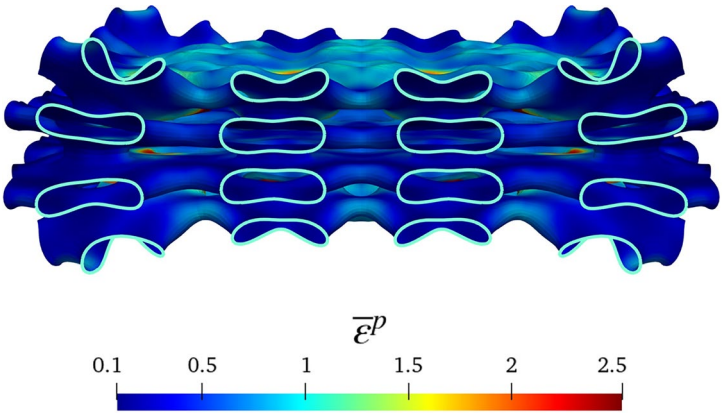

Fig. 10 Equivalent plastic strain plotted on the final configuration of the $4 \times 4 \times 4$ lattice for $\rho = 20\%$ and with no restraining plates

handle such high compression levels without divergence of the computations is a testament to its accuracy and robustness for this problem class. In all cases the experimental results are captured very well in the computations, including for all three regions of interest. The computations appear to be capturing even small fluctuations in the stress history, which are likely tied to the buckling of individual or groups of cells. For the 5% case we ran two cases corresponding to the exact and perturbed geometry (labeled as "Perturbed" on the corresponding plot), which we will discuss in what follows.

Figures 12, 13 and 14 show a sequence of deformed configurations of the TPMS lattice corresponding to the relative densities of 20%, 10% and 5%, respectively. The experimental snapshots of the lattice at the same levels of compression are also shown for comparison.

In Fig. 12, deformations of each unit cell are accurately captured and form a classical "X" shape if one inspects the TPMS core from the side view. The "X" feature is most prominent at 40% strain. A visual inspection reveals various other deformation patterns of unit cells and shows a good correspondence between experiment and simulation. Symmetry about the vertical and horizontal axes is well preserved both in the model and experimental results. The "X" shape is eventually destroyed to accommodate higher levels of compression.

Figure 13 presents the results for the $\rho = 10\%$ case. We again observe a formation of the "X" shape in both the experimental and computational results. However, at about 40% strain, symmetry about the horizontal axis is broken in both simulation and experiment. The experiment predicts bucking of the cells closer to the top, while the simulation predicts bucking of the cells near the bottom plate. These symmetry breaking events manifest themselves in the form of fluctuations in the stress–strain curves in Figure 11, both in the experimental and computational data.

As the shell structures get thinner, they are more prone to imperfection-sensitive behavior [55]. This is clearly illustrated using the $\rho = 5\%$ case shown in Fig. 14. While the overall stress values are predicted well in the computations (see Fig. 11), the deformation patterns between the experimental and computational results are not in such good agreement. Manufacturing flaws or possible asymmetries in the testing procedures result in the immediate loss of symmetry in the experimental results, where the diagonal cells below the horizontal symmetry line collapse first. The simulation results without geometry perturbations do not show this behavior. Instead, a symmetric deformation pattern is maintained until after 40% strain, with minor asymmetries appearing at higher levels of compression.

To trigger the experimentally observed instability, an additional computation was carried out using a 5% reduction in the shell thickness for selected cells in the bottom two rows of the lattice structure. The resulting stress–strain curve in Fig. 11 is labeled "Perturbed". Despite the geometry perturbation, the changes in the stress–strain curve relative to the unperturbed geometry are very minor. However, as may be seen in Fig. 14, the deformed configuration at 20% strain now successfully captures the experimentally observed collapse mode with the bottom two layers of unit cells forming one half of the "X" shape and with the top two layers of unit cells undergoing relatively little deformation. At higher levels of compressive deformation also the top rows of cells eventually collapse.

Figure 15 shows the von Mises stress on the final deformed configuration of the thinnest shell case. The stress is plotted at the shell mid-surface ($\xi_3 = 0$) where only the membrane strains are active. The stress field is quite smooth indicating that there is no issue with membrane locking in the simulations. This is not surprizing because, as mentioned earlier, membrane locking is not expected to occur at this level of shell thickness.

5 Conclusions and future directions

- We introduced the concept of a "minimal patch", which is a key building block of unit cells that comprize sheet TPMS-based lattice structures. The minimal patch ena-

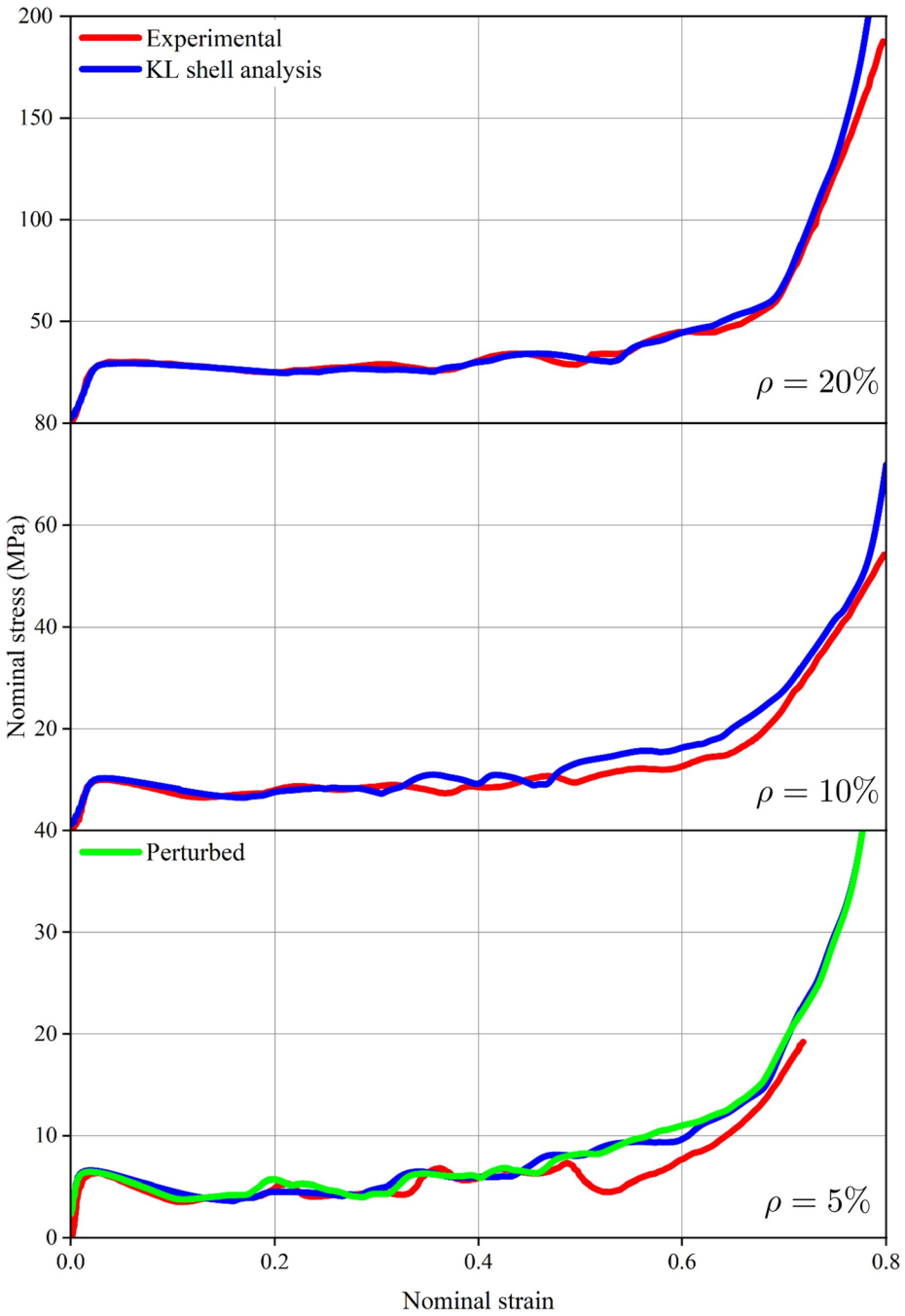

Fig. 11 Nominal stress–strain response of the $4 \times 4 \times 4$ lattices with different relative densities subjected to compressive loading

bles automated construction of NURBS-based IGA-suitable models of these structures.

- The IGA-suitable geometry modeling framework is implemented using a combination of CAD software Rhino and a graphical programming design tool Grasshopper. This approach is flexible, intuitive, minimally invasive and enables the user to establish parametric control over the geometry and mesh resolution of the resulting structural models.
- IGA KL shells are shown to be a robust and accurate computational methodology enabling the assessment of load mitigation performance of sheet TPMS-based structures. The computational models showed remarkable accuracy as measured through comparisons with experimental data for both the prediction of stress–strain responses and the capturing of failure modes of these lattice structures.
- We note that all the computations ran without any convergence issues, reaching the desired levels of lattice compression. This level of robustness is a highly desirable attribute for any physics-based simulation framework employed on a large scale.

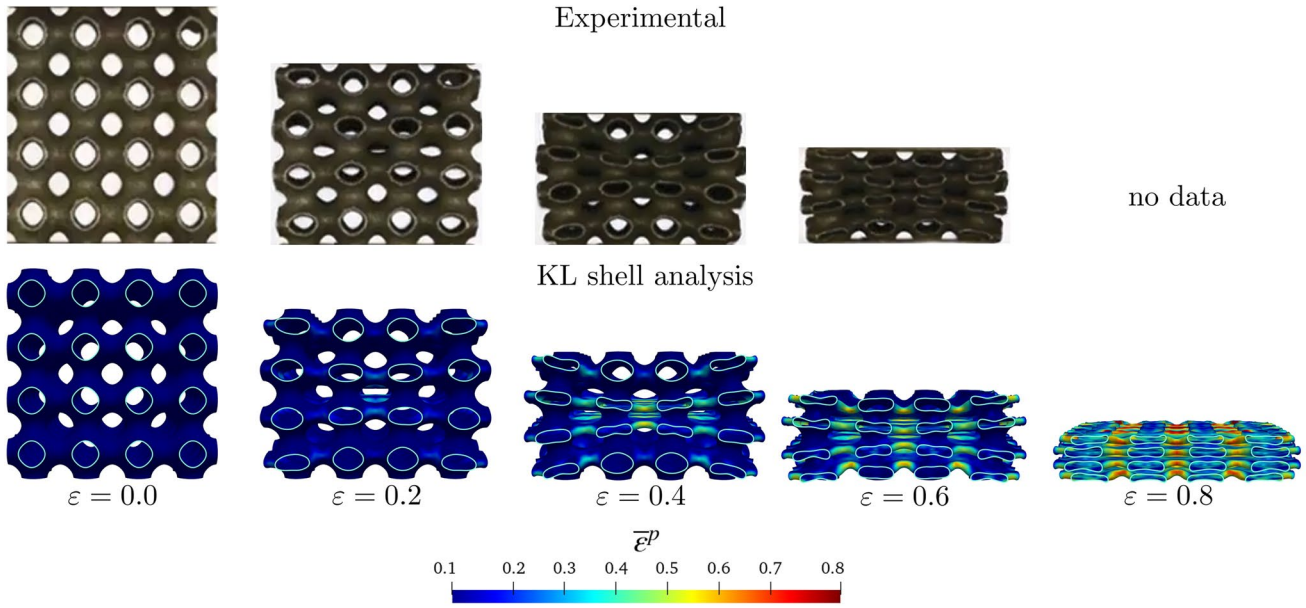

Fig. 12 Sequence of deformed configurations of the $4 \times 4 \times 4$ TPMS lattice corresponding to the relative density of 20%. Comparison of experimental and simulation results. Simulation results show equivalent plastic strain distribution

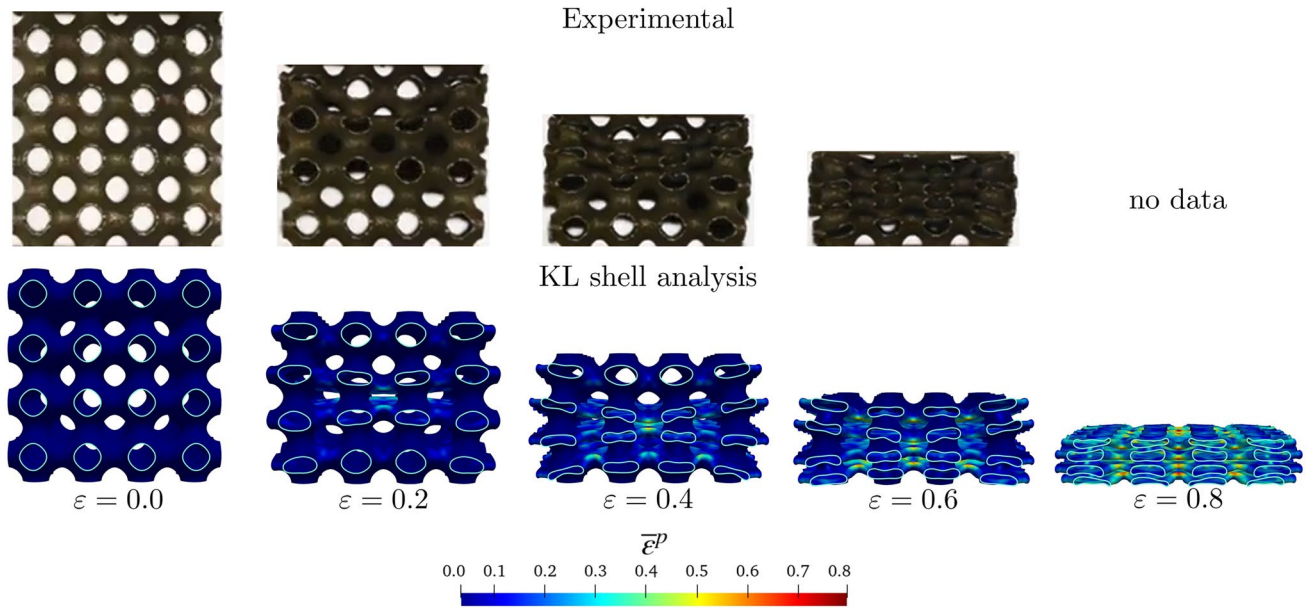

Fig. 13 Sequence of deformed configurations of the $4 \times 4 \times 4$ TPMS lattice corresponding to the relative density of 10%. Comparison of experimental and simulation results. Simulation results show equivalent plastic strain distribution

- There are several extensions and improvements that would benefit the proposed framework. For example, using T-Splines [56, 57] or other unstructured spline technology [58–60] will further increase the efficiency of both the geometry modeling and simulation parts of the framework. Including geometrically and/or functionally graded designs as well as lattices with customizable external shapes will be of paramount importance for real-life applications. Here, ideas developed in [61] may be employed.
- Although the simulations were carried out in a dynamic environment, these were done at relatively slow speeds for consistency with the quasi-static experimental tests carried out in [51]. However, it is of interest to assess the

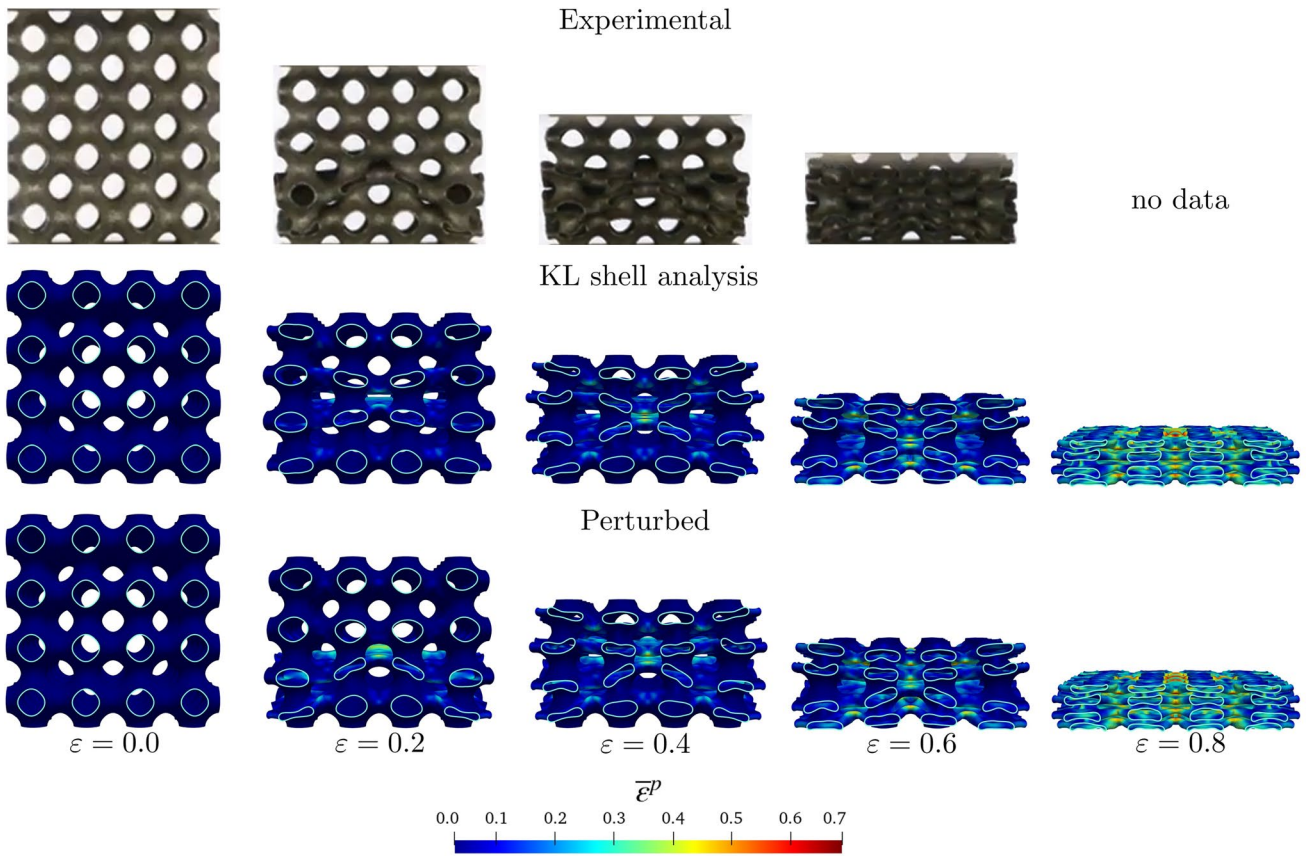

Fig. 14 Sequence of deformed configurations of the $4 \times 4 \times 4$ TPMS lattice corresponding to the relative density of 5%. Comparison of experimental and simulation results. Simulation results show the equivalent plastic strain distribution for both the original and perturbed geometry models

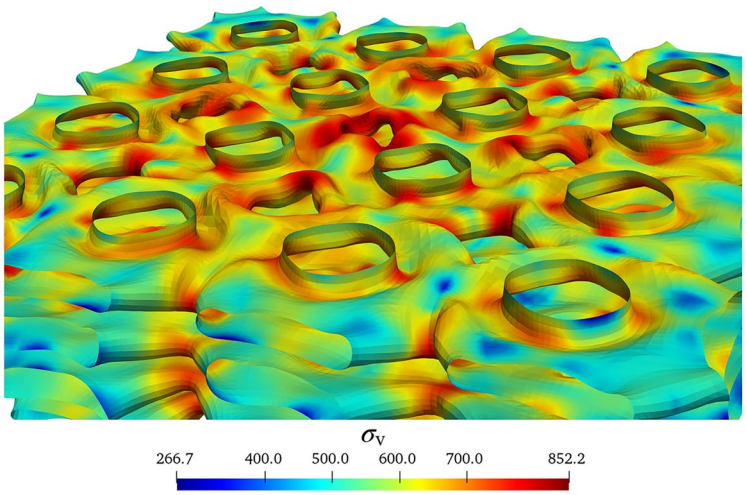

Fig. 15 Mid-surface von Mises stress distribution on the final deformed configuration of the thinnest shell case

behavior of sheet TPMS-based structures at high strain rates in order to assess their ability to mitigate damage due to impact and shock loading. (See, e.g., [62] for recent experimental work on truss-based lattice structures under high strain-rate loading.)

Acknowledgements This work was supported through the ONR Grant No. N00014-21-1-2815.

Authors' contributions K.M. and Y.B. developed the main ideas and finalized technical and implementation details. K.M. carried out the

computer implementation and ran all the test cases. K.M. and Y.B. wrote the manuscript.

Data Availability No datasets were generated or analysed during the current study.

Declarations

Conflict of interest The authors declare no Conflict of interest.

References

1. Ashby MF, Bréchet YJM (2003) Designing hybrid materials. Acta Mater 51(19):5801–5821. https://doi.org/10.1016/S1359-6454(03)00441-5
2. Greer JR, Deshpande VS (2019) Three-dimensional architected materials and structures: design, fabrication, and mechanical behavior. MRS Bull 44(10):750–757. https://doi.org/10.1557/mrs.2019.232
3. Xia X, Afshar A, Yang H, Portela CM, Kochmann DM, Di Leo CV, Greer JR (2019) Electrochemically reconfigurable architected materials. Nature 573(7773):205–213. https://doi.org/10.1038/s41586-019-1538-z
4. Kochmann DM, Bertoldi K (2017) Exploiting microstructural instabilities in solids and structures: from metamaterials to structural transitions. Appl Mech Rev 69(5):050801. https://doi.org/10.1115/1.4037966
5. O'Masta MR, Dong L, St-Pierre L, Wadley HNG, Deshpande VS (2017) The fracture toughness of octet-truss lattices. J Mech Phys Solids 98:271–289. https://doi.org/10.1016/j.jmps.2016.09.009
6. Shaikeea AJD, Cui H, O'Masta M, Zheng XR, Deshpande VS (2022) The toughness of mechanical metamaterials. Nat Mater 21(3):297–304. https://doi.org/10.1038/s41563-021-01182-1
7. Meza LR, Zelhofer AJ, Clarke N, Mateos AJ, Kochmann DM, Greer JR (2015) Resilient 3D hierarchical architected metamaterials. Proc Natl Acad Sci 112(37):11502–11507. https://doi.org/10.1073/pnas.1509120112
8. Cheng G, Miao C, Qin Q, Li J, Xu F, Haftbaradaran H, Dickey EC, Gao H, Zhu Y (2015) Large anelasticity and associated energy dissipation in single-crystalline nanowires. Nat Nanotechnol 10(8):687–691. https://doi.org/10.1038/nnano.2015.135
9. Chen I-T, Poblete FR, Bagal A, Zhu Y, Chang C-H (2022) Anelasticity in thin-shell nanolattices. Proc Natl Acad Sci 119(38):2201589119. https://doi.org/10.1073/pnas.2201589119
10. Lin Z, Novelino LS, Wei H, Alderete NA, Paulino GH, Espinosa HD, Krishnaswamy S (2020) Folding at the microscale: enabling multifunctional 3D origami-architected metamaterials. Small 16(35):2002229. https://doi.org/10.1002/smll.202002229
11. Schoen AH (1970) Infinite periodic minimal surfaces without self-intersections. Technical report
12. Attarzadeh R, Rovira M, Duwig C (2021) Design analysis of the "Schwartz D'' based heat exchanger: a numerical study. Int J Heat Mass Transf 177:121415. https://doi.org/10.1016/j.ijheatmasstransfer.2021.121415
13. Baena-Moreno FM, González-Castaño M, Navarro de Miguel JC, Miah KUM, Ossenbrink R, Odriozola JA, Arellano-García H (2021) Stepping toward efficient microreactors for CO2 methanation: 3D-printed gyroid geometry. ACS Sustain Chem Eng 9(24):8198–8206. https://doi.org/10.1021/acssuschemeng.1c01980
14. Tikhonov A, Evdokimov P, Klimashina E, Tikhonova S, Karpushkin E, Scherbackov I, Dubrov V, Putlayev V (2020) Stereolithographic fabrication of three-dimensional permeable scaffolds from CaP/PEGDA hydrogel biocomposites for use as bone grafts. J Mech Behav Biomed Mater 110:103922. https://doi.org/10.1016/j.jmbbm.2020.103922
15. Yin H, Liu Z, Dai J, Wen G, Zhang C (2020) Crushing behavior and optimization of sheet-based 3D periodic cellular structures. Compos Part B Eng 182:107565. https://doi.org/10.1016/j.compositesb.2019.107565
16. Timoshenko S, Woinowsky-Krieger S et al (1959) Theory of plates and shells, vol 2. McGraw-Hill, New York
17. Hughes TJR, Cottrell JA, Bazilevs Y (2005) Isogeometric analysis: CAD, finite elements, NURBS, exact geometry and mesh refinement. Comput Methods Appl Mech Eng 194(39–41):4135–4195. https://doi.org/10.1016/j.cma.2004.10.008
18. Cottrell JA, Hughes TJR, Bazilevs Y (2009) Isogeometric analysis: toward integration of CAD and FEA. Wiley, NewYork
19. Kiendl J, Bletzinger K-U, Linhard J, Wüchner R (2009) Isogeometric shell analysis with Kirchhoff–Love elements. Comput Methods Appl Mech Eng 198(49–52):3902–3914. https://doi.org/10.1016/j.cma.2009.08.013
20. Benson DJ, Bazilevs Y, Hsu MC, Hughes TJR (2010) Isogeometric shell analysis: The Reissner–Mindlin shell. Comput Methods Appl Mech Eng 199(5–8):276–289. https://doi.org/10.1016/j.cma.2009.05.011
21. Hughes TJ (2012) The finite element method: linear static and dynamic finite element analysis. Courier Corporation, North Chelmsford
22. Belytschko T, Liu WK, Moran B, Elkhodary KI (2014) Nonlinear finite elements for continua and structures, 2nd edn. Wiley, New York
23. Piegl L, Tiller W (1996) The NURBS book. Springer, New York
24. Schwarz HA (1972) Gesammelte mathematische abhandlungen, vol 260. American Mathematical Society, Providence
25. Lord EA, Mackay AL (2003) Periodic minimal surfaces of cubic symmetry. Curr Sci 85(3):346–362
26. Gandy PJF, Klinowski J (2000) Exact computation of the triply periodic Schwarz P minimal surface. Chem Phys Lett 322(6):579–586. https://doi.org/10.1016/S0009-2614(00)00453-X
27. Hsu M-C, Wang C, Herrema AJ, Schillinger D, Ghoshal A, Bazilevs Y (2015) An interactive geometry modeling and parametric design platform for isogeometric analysis. Comput Math Appl 70(7):1481–1500. https://doi.org/10.1016/j.camwa.2015.04.002
28. Robert McNeel & Associates: Rhinoceros. https://www.rhino3d.com/. Accessed: 14 June 2022 (2023)
29. Robert McNeel & Associates: Grasshopper. https://www.grasshopper3d.com/. Accessed: 14 June 2022 (2023)
30. Feng J, Fu J, Shang C, Lin Z, Li B (2018) Porous scaffold design by solid T-splines and triply periodic minimal surfaces. Comput Methods Appl Mech Eng 336:333–352. https://doi.org/10.1016/j.cma.2018.03.007
31. Benson DJ, Bazilevs Y, Hsu M-C, Hughes TJR (2011) A large deformation, rotation-free, isogeometric shell. Comput Methods Appl Mech Eng 200(13–16):1367–1378. https://doi.org/10.1016/j.cma.2010.12.003
32. Benson DJ, Hartmann S, Bazilevs Y, Hsu M-C, Hughes TJR (2013) Blended isogeometric shells. Comput Methods Appl Mech Eng 255:133–146. https://doi.org/10.1016/j.cma.2012.11.020
33. Hosseini S, Remmers JJC, Verhoosel CV, De Borst R (2013) An isogeometric solid-like shell element for nonlinear analysis. Int J Numer Methods Eng 95(3):238–256. https://doi.org/10.1002/nme.4505
34. Bouclier R, Elguedj T, Combescure A (2015) An isogeometric locking-free NURBS-based solid-shell element for geometrically nonlinear analysis: an isogeometric locking-free NURBS-based solid-shell element for geometrically nonlinear analysis. Int J Numer Methods Eng 101(10):774–808. https://doi.org/10.1002/nme.4834

35. Morganti S, Auricchio F, Benson DJ, Gambarin FI, Hartmann S, Hughes TJR, Reali A (2015) Patient-specific isogeometric structural analysis of aortic valve closure. Comput Methods Appl Mech Eng 284:508–520. https://doi.org/10.1016/j.cma.2014.10.010
36. Cirak F, Ortiz M, Schroder P (2000) Subdivision surfaces: a new paradigm for thin-shell finite-element analysis. Int J Numer Methods Eng 47(12):2039–2072. https://doi.org/10.1002/(SICI)1097-0207(20000430)47:12<2039::AID-NME872>3.0.CO;2-1
37. Behzadinasab M, Alaydin M, Trask N, Bazilevs Y (2022) A general-purpose, inelastic, rotation-free Kirchhoff–Love shell formulation for peridynamics. Comput Methods Appl Mech Eng 389:114422. https://doi.org/10.1016/j.cma.2021.114422
38. Alaydin MD, Benson DJ, Bazilevs Y (2021) An updated Lagrangian framework for Isogeometric Kirchhoff–Love thin-shell analysis. Comput Methods Appl Mech Eng 384:113977. https://doi.org/10.1016/j.cma.2021.113977
39. Ahmad S, Irons BM, Zienkiewicz OC (1970) Analysis of thick and thin shell structures by curved finite elements. Int J Numer Methods Eng 2(3):419–451. https://doi.org/10.1002/nme.1620020310
40. Bischoff M (2018) Finite elements for plates and shells. In: Altenbach H, Öchsner A (eds) Encyclopedia of continuum mechanics. Springer, Berlin, pp 1–23. https://doi.org/10.1007/978-3-662-53605-6_14-1
41. Flanagan DP, Taylor LM (1987) An accurate numerical algorithm for stress integration with finite rotations. Comput Methods Appl Mech Eng 62(3):305–320. https://doi.org/10.1016/0045-7825(87)90065-x
42. Kamensky D, Xu F, Lee C-H, Yan J, Bazilevs Y, Hsu M-C (2018) A contact formulation based on a volumetric potential: application to isogeometric simulations of atrioventricular valves. Comput Methods Appl Mech Eng 330:522–546. https://doi.org/10.1016/j.cma.2017.11.007
43. Herrema AJ, Johnson EL, Proserpio D, Wu MCH, Kiendl J, Hsu M-C (2019) Penalty coupling of non-matching isogeometric Kirchhoff–Love shell patches with application to composite wind turbine blades. Comput Methods Appl Mech Eng 346:810–840. https://doi.org/10.1016/j.cma.2018.08.038
44. Leidinger LF, Breitenberger M, Bauer AM, Hartmann S, Wüchner R, Bletzinger K-U, Duddeck F, Song L (2019) Explicit dynamic isogeometric B-Rep analysis of penalty-coupled trimmed NURBS shells. Comput Methods Appl Mech Eng 351:891–927. https://doi.org/10.1016/j.cma.2019.04.016
45. Kiendl J, Bazilevs Y, Hsu M-C, Wüchner R, Bletzinger K-U (2010) The bending strip method for isogeometric analysis of Kirchhoff–Love shell structures comprised of multiple patches. Comput Methods Appl Mech Eng 199(37–40):2403–2416. https://doi.org/10.1016/j.cma.2010.03.029
46. Brivadis E, Buffa A, Wohlmuth B, Wunderlich L (2015) Isogeometric mortar methods. Comput Methods Appl Mech Eng 284:292–319. https://doi.org/10.1016/j.cma.2014.09.012
47. Apostolatos A, Breitenberger M, Wüchner R, Bletzinger K-U (2015) Domain decomposition methods and Kirchhoff–Love shell multipatch coupling in isogeometric analysis. In: Jüttler B, Simeon B (eds) Isogeometric Analysis and Applications 2014, vol 107. Springer International Publishing, Cham, pp 73–101. https://doi.org/10.1007/978-3-319-23315-4_4
48. Guo Y, Heller J, Hughes TJR, Ruess M, Schillinger D (2018) Variationally consistent isogeometric analysis of trimmed thin shells at finite deformations, based on the STEP exchange format. Comput Methods Appl Mech Eng 336:39–79. https://doi.org/10.1016/j.cma.2018.02.027
49. Nguyen-Thanh N, Zhou K, Zhuang X, Areias P, Nguyen-Xuan H, Bazilevs Y, Rabczuk T (2017) Isogeometric analysis of large-deformation thin shells using RHT-splines for multiple-patch coupling. Comput Methods Appl Mech Eng 316:1157–1178. https://doi.org/10.1016/j.cma.2016.12.002
50. Fu J, Qu S, Ding J, Song X, Fu MW (2021) Comparison of the microstructure, mechanical properties and distortion of stainless steel 316 L fabricated by micro and conventional laser powder bed fusion. Addit Manuf 44:102067. https://doi.org/10.1016/j.addma.2021.102067
51. Fu J, Ding J, Qu S, Zhang L, Wang MY, Fu MW, Song X (2022) Improved light-weighting potential of SS316L triply periodic minimal surface shell lattices by micro laser powder bed fusion. Mater Des 222:111018. https://doi.org/10.1016/j.matdes.2022.111018
52. Casquero H, Mathews KD (2023) Overcoming membrane locking in quadratic NURBS-based discretizations of linear Kirchhoff–Love shells: CAS elements. Comput Methods Appl Mech Eng 417:116523. https://doi.org/10.1016/j.cma.2023.116523
53. Yin H, Zheng X, Wen G, Zhang C, Wu Z (2021) Design optimization of a novel bio-inspired 3D porous structure for crashworthiness. Compos Struct 255:112897. https://doi.org/10.1016/j.compstruct.2020.112897
54. Wang Z, Wang X, Gao T, Shi C (2021) Mechanical behavior and deformation mechanism of triply periodic minimal surface sheet under compressive loading. Mech Adv Mater Struct 28(19):2057–2069. https://doi.org/10.1080/15376494.2020.1829756
55. Gerasimidis S, Virot E, Hutchinson JW, Rubinstein SM (2018) On establishing buckling knockdowns for imperfection-sensitive shell structures. J Appl Mech 85(9):091010. https://doi.org/10.1115/1.4040455
56. Bazilevs Y, Calo VM, Cottrell JA, Evans JA, Hughes TJR, Lipton S, Scott MA, Sederberg TW (2010) Isogeometric analysis using T-splines. Comput Methods Appl Mech Eng 199(5–8):229–263. https://doi.org/10.1016/j.cma.2009.02.036
57. Casquero H, Wei X, Toshniwal D, Li A, Hughes TJR, Kiendl J, Zhang YJ (2020) Seamless integration of design and Kirchhoff–Love shell analysis using analysis-suitable unstructured T-splines. Comput Methods Appl Mech Eng 360:112765. https://doi.org/10.1016/j.cma.2019.112765
58. Giannelli C, Jüttler B, Speleers H (2012) THB-splines: the truncated basis for hierarchical splines. Comput Aid Geo Des 29(7):485–498. https://doi.org/10.1016/j.cagd.2012.03.025
59. Johannessen KA, Kvamsdal T, Dokken T (2014) Isogeometric analysis using LR B-splines. Comput Methods Appl Mech Eng 269:471–514. https://doi.org/10.1016/j.cma.2013.09.014
60. Thomas DC, Engvall L, Schmidt SK, Tew K, Scott MA (2022) U-splines: splines over unstructured meshes. Comput Methods Appl Mech Eng 401:115515. https://doi.org/10.1016/j.cma.2022.115515
61. Antolin P, Buffa A, Cohen E, Dannenhoffer JF, Elber G, Elgeti S, Haimes R, Riesenfeld R (2019) Optimizing micro-Tiles in microstructures as a design paradigm. Comput-Aid Des 115:23–33. https://doi.org/10.1016/j.cad.2019.05.020
62. Weeks JS, Gandhi V, Ravichandran G (2022) Shock compression behavior of stainless steel 316L octet-truss lattice structures. Int J Impact Eng 169:104324. https://doi.org/10.1016/j.ijimpeng.2022.104324